Solar RRL
www.solar-rrl.com

Laser-Assisted Nanotexturing for Flexible Ultrathin Crystalline Si Solar Cells

Youngseok Lee, Jeong-Hyun Woo, Keonhee Kim, Kyeong Seok Lee, Yeonjoo Jeong, Jaewook Kim, Gyu Weon Hwang, Doh-Kwon Lee, Ju-Young Kim, and Inho Kim**

Ultrathin (UT) crystalline Si wafers, which are more flexible than conventional ones, can apply to curved surfaces, enabling a wide range of applications such as building-integrated photovoltaics, vehicle-integrated photovoltaics, and wearable devices. Thinner wafers require more effective light trapping; thus, surface texturing in microscale is a common approach to compensate for the reduced thickness by enhancing the light pathlength. Microscale textures, however, deteriorate the mechanical flexibility due to stress concentration in the valley of the microtextures. In this study, a laser-assisted nanotexturing process is proposed for enhanced flexibility of the UT Si solar cells with a 50 μm thickness while maintaining light-trapping performances. A nanolens array is used to focus laser onto the Si wafers, inducing the formation of nanoparticle etch masks for nanopyramid texturing in an alkaline solution. The origin of the enhanced flexibility of the nanotextured Si wafers is discussed by a micromechanics simulation study. Herein, nanotexturing technique is applied to UT Si-based passivated emitter rear cells and the enhanced flexibility of the cells with a 26 mm critical bending radius is demonstrated. Also, it is shown that the nanotextured Si wafer provides a higher efficiency of 18.68%, whereas the microtextured one exhibits 18.10%.

1. Introduction

Ultrathin (UT) crystalline silicon (c-Si) solar cells with a thickness below 50 μm have recently attracted increased attention due to their properties of being thin, lightweight, and bendable,[1,2] making them well suited for use in applications where a solar module weight is a significant factor like building-integrated photovoltaics, vehicle-integrated photovoltaics, and wearable electronics. However, as the thickness of Si wafers decreases, more effective light-trapping techniques and stronger surface passivation are required to maintain a high efficiency, which is one of the most challenging issues for UT–Si-based solar cell development.

The cost of Si has demonstrated some fluctuations in the past due to rapid demand growth and limited manufacturing capabilities.[3] However, Si wafers currently account for an average of 14% to the total module production cost.[4] Therefore, reducing the Si wafer thickness is economically beneficial to decrease the amount of Si utilized in solar cells by reducing the Si wafer thickness.[5] However, due to the indirect semiconductor nature of crystalline Si, it exhibits poor absorption for low-energy photons.[6] To minimize optical absorption loss over a broad spectral range, surface texturing is required to increase the optical path length of light within Si wafers.

Y. Lee,[+] K. Kim, K. S. Lee, Y. Jeong, J. Kim, G. W. Hwang, I. Kim
Center for Neuromorphic Engineering
Korea Institute of Science and Technology (KIST)
Seoul 02792, Republic of Korea
E-mail: inhok@kist.re.kr

J.-H. Woo
Disposal Safety Evaluation Research Division
Korea Atomic Energy Research Institute (KAERI)
Daejeon 34057, Republic of Korea

The ORCID identification number(s) for the author(s) of this article can be found under https://doi.org/10.1002/solr.202300376.

[+]Present address: Cell R&D Team, Hanhwa Q Cells, 202, Sandsuandan 2-ro, Jincheon-gun, Republic of Korea

DOI: 10.1002/solr.202300376

K. Kim
Department of Electrical Engineering
Korea University
Seoul 02841, Republic of Korea

D.-K. Lee
Advanced Photovoltaics Research Center
Korea Institute of Science and Technology (KIST)
Seoul 02792, Republic of Korea

D.-K. Lee
School of Advanced Materials Science and Engineering
Sungkyunkwan University
Suwon, Gyeonggi-do 16419, Republic of Korea

J.-Y. Kim
Department of Materials Science and Engineering
Ulsan National Institute of Science and Technology (UNIST)
Ulsan 44919, Republic of Korea
E-mail: juyoung@unist.ac.kr

Recently, there have been many attempts to manufacture Si solar cells with UT c-Si wafers with a thickness of less than 50 μm to achieve flexible solar cells by reducing the rigidity of Si wafers.[7–12] However, UT c-Si wafers without antireflection treatment exhibit extreme light absorption losses of over 30% across the entire wavelength range due to the refractive index mismatch between air and crystalline Si. Additionally, UT c-Si exhibits a drastic absorption loss at wavelengths exceeding 900 nm due to its low absorption coefficient.[1] Since the long wavelength region exceeding 900 nm of sunlight constitutes approximately 18% of the solar radiation energy, improving the absorption of such long-wavelength light in the UT c-Si solar cells is critical to achieving high efficiency. Although nano- and microstructures have been used to texture UT c-Si solar cells and shown efficiencies as high as 18.9%,[13] they present challenges such as complicated fabrication processes and severe recombination of minority carriers. For improved light trapping in UT c-Si wafers, surface texturing using periodic nanostructured arrays such as nanowires,[14] nanocones,[1] nanopencils,[15] and nanopyramids[16,17] has been used and have the potential to approach the Lambertian absorption limit.[18] In terms of textures, small pyramidal textures in the range of sub-micrometer can improve photocurrent by effectively increasing the overall path length of light propagation in c-Si wafers. However, it is difficult to produce micropyramid textures in the 3–10 μm range while securing high production yield in the case of UT c-Si solar cells. This is because the UT c-Si wafers with a thickness comparable to the texture size becomes fragile due to the stress concentration on the deep valleys of the micropyramids.[19] In contrast, small pyramidal textures in the sub-micrometer range are more compatible with UT c-Si solar cell fabrication processes.[20] It is important to note that the surface structures could function as crack initiation sites where the mechanical stress can concentrate, significantly degrading the flexibility of UT c-Si solar cells. Therefore, there is a need to develop new light-trapping strategies that can enhance the light absorption in the entire wavelength region while maintaining the stable flexibility of the UT c-Si solar cells.

Most studies investigating nanostructures on c-Si wafers have focused on direct pattering using nanolithography techniques such as e-beam lithography,[21–23] laser interference lithography,[24,25] and nanoimprint lithography[26,27] to produce the aforementioned nanostructures. However, these methods are not commercially viable for large area solar cell production due to high production costs (Table S1, Supporting Information). Laser-texturing techniques have advantages over other nanotexturing techniques because they are cost-effective and highly compatible with Si solar cell processes. A lot of research has been carried out on a laser-texturing technique and its application for Si solar cells since it was first demonstrated by Zopler et al.[28] The ultrashort pulse laser in nanosecond was used to pattern Si wafers by direct writing in micrometer scale periodicity.[29,30] For nanoscale texturing, the shorter pulse laser in femtosecond to picosecond was used for texturing of crystalline Si wafers without any masks. Monocrystalline or multi-crystalline Si wafers are irradiated in the air or reactive atmosphere of SF_6 by high-energy pulse laser and form nanostructures of various shapes such as sharp spikes, cones, and flakes.[31,32] This is one of the black Si-texturing techniques. Although there have been many studies on black Si texturing using the ultrashort pulse laser, high efficiency solar cells have been rarely reported.[33,34] One of the main reasons for this is the laser damage to the wafer and challenges in surface passivation. Also, the size or period of the nanostructure is very difficult to modulate because it is a mask-less process. In addition, while there are many prior studies on the application of the nanostructures to UT–Si wafers as a means to increase the light absorption of UT–Si, only a few have examined their impact on the mechanical strength of UT c-Si solar cells.[8,13,17,35,36]

In this study, we present a novel process for nanotexturing c-Si wafers using a nanolens array and a nanosecond pulse laser. The laser was focused through the nanolens onto the 50 μm thick UT-Si wafers, inducing localized heating and forming silicon oxide, which served as nanoetch masks for producing nanopyramid texturing. The processed Si wafers were dipped in the alkaline chemical solution for nanoscale pyramidal texturing. During this process, the laser damage is nearly completely removed, and the surface textures of a pyramidal shape can be more easily passivated compared with the high aspect ratio structures of the black Si textures. Also, the size and period of the pyramids can be tuned by using a nanolens array of varying periods. This will provide room for more efficient light trapping. The resulting nanotextured UT c-Si wafers exhibited comparable light-trapping performances to microtextured ones. Furthermore, the nanotextured UT c-Si wafers showed enhanced mechanical flexibility, which was revealed by a four-point bending test. We conducted a mechanics simulation study to reveal the origin of the enhanced flexibility. Finally, we successfully produced the flexible UT c-Si solar cells using the laser-assisted texturing technique developed in this study. We analyzed and discussed the device performances and flexibility of the UT c-Si solar cells.

2. Results

2.1. Laser-Assisted Nanotexturing Process

The process of nanopyramid-texturing process using a nanosecond pulse laser is illustrated in **Figure 1** and consists of three main steps: 1) nanolens fabrication, 2) laser processing, and 3) pyramid texturing in an alkaline solution as illustrated. The first step involves the fabrication of a hydrogen silsesquioxane (HSQ) nanolens with a convex optical structure, which is prepared through a sequential process of silica nanosphere (SNS) lithography and nanoimprint lithography (NIL). In the second step, the nanolens is placed on the c-Si wafer and irradiated with a nanosecond pulse laser to form nanoparticle etch masks on the surface of the c-Si wafers. Finally, in the third step, a typical KOH etching process is conducted to form nanopyramidal structures on the c-Si wafers.

2.2. Nanolens Fabrication Results

For the laser-assisted texturing process, a nanolens was utilized, which was obtained through an NIL process after producing a Si master sample via SNS lithography. **Figure 2**a illustrates the process of coating silica spheres onto the surface of the Si wafer for SNS lithography, followed by the reactive ion etching (RIE)

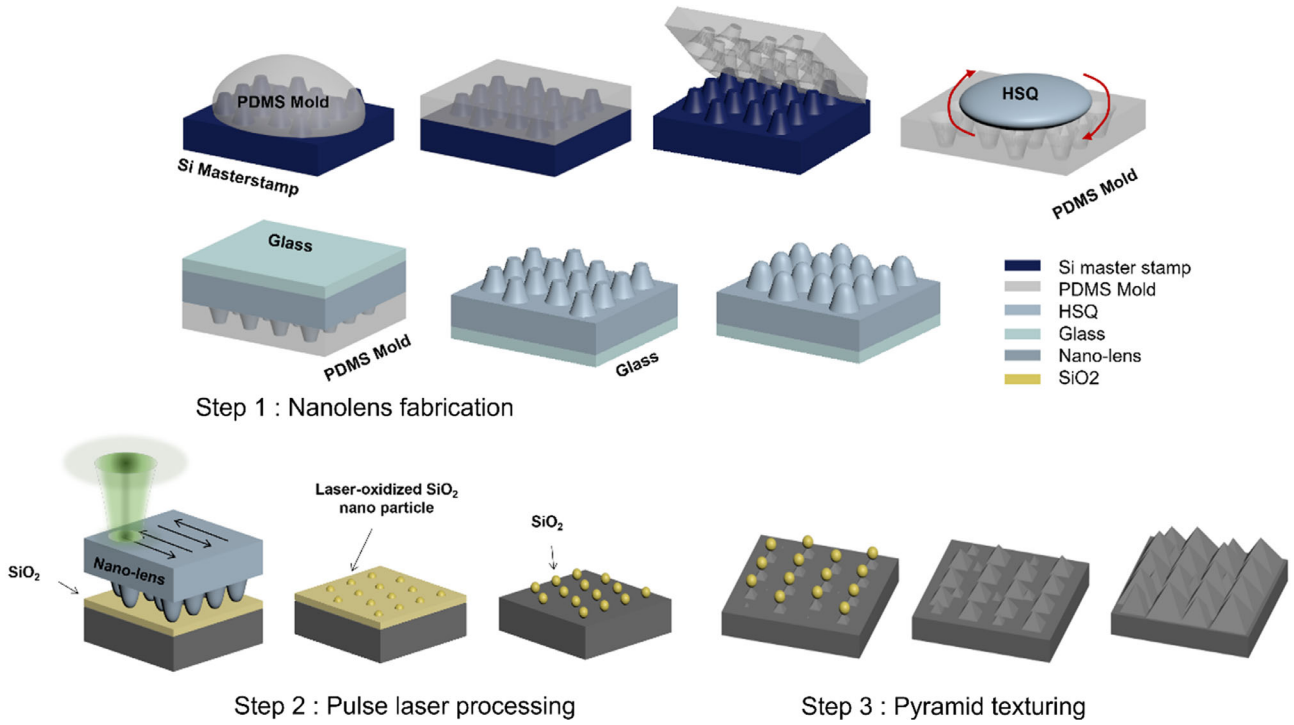

Figure 1. The overall process flow of laser assisted texturing using nanolens. Step 1: polydimethylsiloxane (PDMS) pouring into a Si master stamp, baking process, detaching PDMS mold, hydrogen silsesquioxane (HSQ) resin–coating process for nanolens fabrication, replication of PDMS mold with nano-imprint, and post-process for refining the final shape of the nanolens and curing. Step 2: scanning of pulse laser to induce nanoparticles, hydrofluoric acid (HF) treatment. Step 3: KOH texturing in an alkaline solution, finished pyramid texturing after enough etching time.

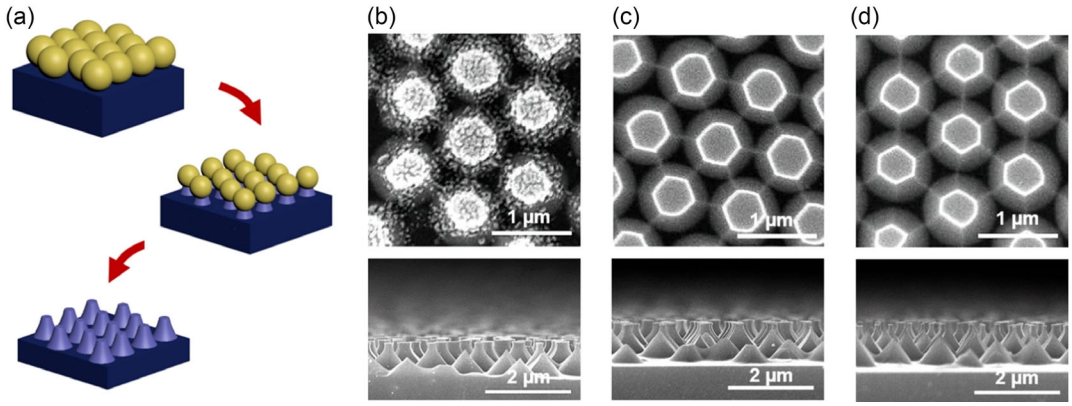

Figure 2. Silicon master sample image used for nanolens fabrication: a) a schematic diagram of the silicon master sample manufacturing process through silica bead coating and reactive ion etching (RIE) process, b) the RIE process is performed by mixing SF_6 and O_2 gas, and top-view and cross-view images of the silicon etching surface when the partial pressure ratio of O_2 gas is 10%, c) etched images when using O_2 gas partial pressure ratio of 20%, and d) etched images when using O_2 gas partial pressure ratio of 30%.

process to generate Si nanostructures for the master sample. SF_6 and O_2 gases were used for RIE, and the shape of the nanostructures was adjusted by varying the partial pressure ratio of O_2 gas.[37] Since the nanolens array was fabricated by replicating the Si master sample, the shape of the master sample needed to be optimized for the effective light focusing. As demonstrated in Figure 2b, the surface of the silicon wafer that underwent the RIE process for 5 min under the condition of 10% O_2 partial pressure was rough and therefore excluded from the master sample. The 20% O_2 partial pressure ratio was chosen as the most suitable condition, as the surface of the master sample was smooth, and the lens shape was not too narrow, as illustrated in Figure 2c. In contrast, the condition of 30% O_2 partial pressure ratio was not suitable as a master sample, as the lens shape was too narrow, as shown in Figure 2d.

This master sample was coated with polydimethylsiloxane (PDMS) to make a pattern, and a nanolens was manufactured through HSQ resin and NIL process.[38] To further modify the

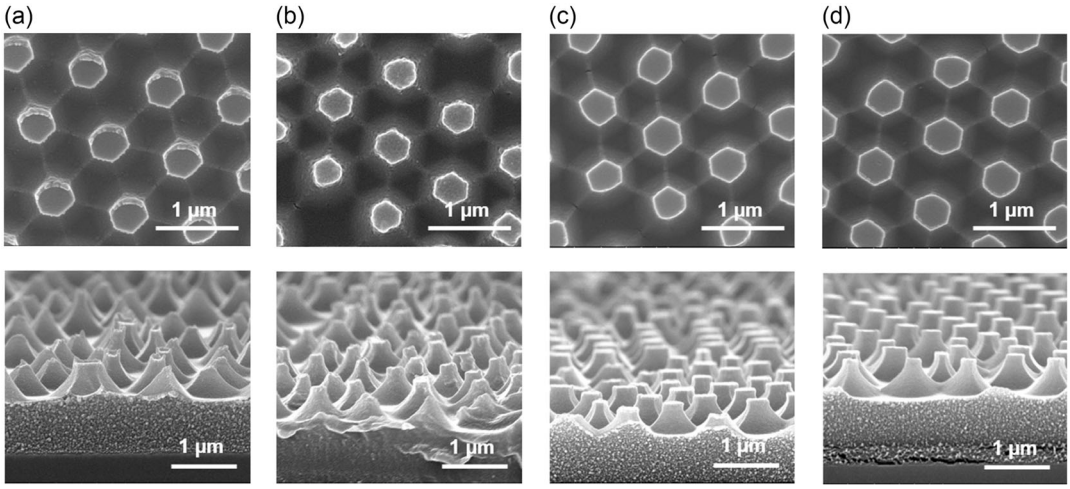

Figure 3. Scanning electron microscope (SEM) images of nanolens formed on a glass substrate through the nanoimprint method: a) images of nanolens after nanoimprint and without post-processing, b) images of nanolens with only 60 min of curing without UV treatment, c) images of nanolenses after 30 min of UV treatment and 60 min of curing, and d) images of nanolenses after 60 min of UV treatment and 60 min of curing.

shape of the nanolens, additional UV and heat treatments at 400 °C for 1 h were performed. There was a change in the shape of the nanolens due to the UV treatment process, while the shape of the HSQ film without UV treatment easily collapsed as shown in **Figure 3**a,b. As the UV treatment time increased to 30 min and 1 h, the shape of the nanolens was well maintained after the HSQ curing as seen in Figure 3c,d. After 1 h of the UV treatment and 1 h of the heat treatment at 400 °C, the shape of the nanolens as shown in Figure 3d showed nearly the same as that of the Si master sample, and thus this condition was used for the nanolens fabrication. The completed HSQ nanolens has a hexagonal arrangement of flat hexagonal heads with about 800 nm, as shown in Figure 3d. The height of each lens column was about 1 μm.

2.3. Laser-Assisted Texturing Process

The fabricated nanolens, serving as a focusing lens, was placed on a Si wafer with a size of 30 × 30 mm, and the entire area was irradiated using a scanning pulse laser. Prior to laser irradiation, a 90 nm thick SiO_2 layer was deposited on the Si wafers by plasma-enhanced chemical vapor deposition (PECVD). The SiO_2 layer plays a crucial role in reducing optical reflection from the Si surface and increasing the optical absorption in the Si wafers, as evidenced by the FDTD simulation results in Figure S1, Supporting Information.[39] Following laser irradiation, the Si wafers were dipped in a hydrofluoric acid (HF) solution to remove the SiO_2 layer, and then textured through the KOH solution, which is commonly used for Si pyramid texturing. Refer to the overall laser-assisted texturing process as illustrated in Figure 1.

The surface of the Si wafers after the laser irradiation was examined using electron microscopy and is shown in **Figure 4**a–f. The most crucial part of the laser-assisted texturing process is the use of a nanolens to focus the laser beam on the surface of SiO_2/Si to creating unique nanoparticles on the Si surface by inducing local heating on the Si wafer surface. The appearance of these nanoparticles was confirmed through scanning electron microscope (SEM) images in Figure 4a. Most nanoparticles remained even after HF treatment as seen in Figure 4b. The SEM image in Figure 4c confirmed that the average size of the spherical nanoparticles was approximately 400 nm. These nanoparticles function as etch masks when Si wafers are textured in a KOH solution, facilitating fast and dense pyramid nucleation at the beginning of the texture reaction. Figure 4d shows that, by this mechanism, a Si surface with uniform and dense nanopyramids was obtained even with a short etching time of only 90 s. A small etch loss, combined with a shorter etch time, would be more advantageous for 50 μm thick UT c-Si wafers. The magnified SEM images of the textured samples in plan and cross-sectional view show that the produced pyramids are all sub-micrometer in scale, as depicted in Figure 4e,f. The origin of the nanoparticles induced by laser was analyzed by X-ray photoelectron spectroscopy (XPS). For a comparative study, two Si wafers were deposited with 100 nm thick SiO_2 thin films. One wafer was subjected to the laser process while the other remained intact. Subsequently, both wafers were treated in an HF solution for 2 min to remove the SiO_2 thin film, and XPS spectra were taken. The XPS spectra in Figure 4g–h revealed that a [Si]/[O] ratio and a Si–O bond peak increased after laser irradiation, supporting that the nanoparticles are made of SiO_2 and generated by a laser passed through the nanolens. The detailed values of the characteristic peaks in the XPS spectra are summarized in **Table 1**. To investigate the effect of the nanolens for laser focusing, the same laser-processing experiment without nanolens was conducted on SiO_2-coated Si wafers. We observed that the formation of the SiO_2 nanoparticles was greatly suppressed, and as a result, the pyramid textures were nonuniformly formed and the texturing could not be completed at a given process time of 90 s. The SEM images of the Si wafers for the laser-assisted texturing cases with and without nanolens are presented in Figure S2, Supporting Information, for reference with different texturing process time.

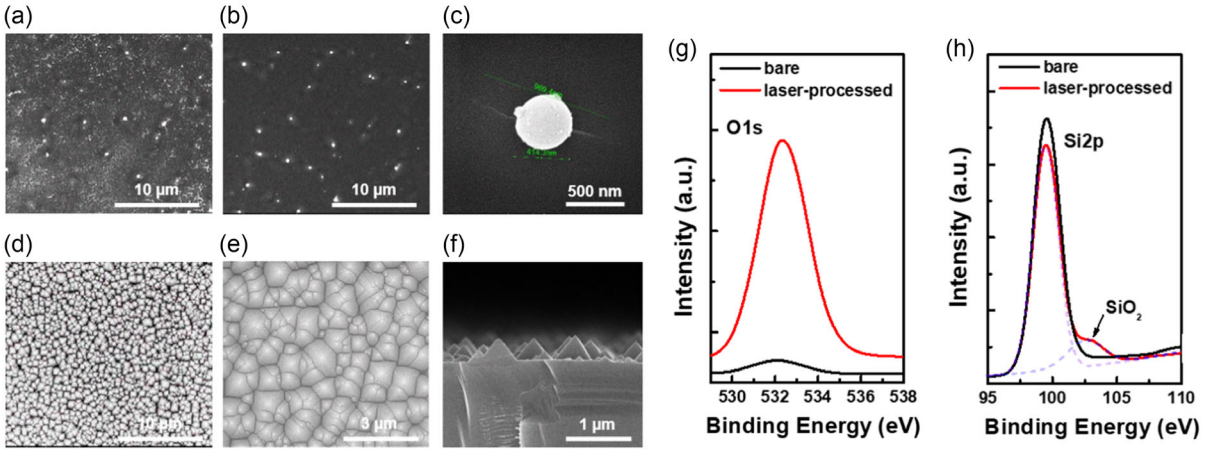

Figure 4. a) SEM image of the surface of a untreated bare Si wafer, b) SEM image of a laser-processed Si wafer, c) SEM image of a laser-induced nanoparticle on the laser-processed Si wafer, d) SEM image of the surface of the laser-processed Si wafer after 90 s of KOH etching, e) magnified SEM image of the textured Si wafer, f) magnified SEM image of the textured Si wafer in cross-sectional view, g) X-ray photoelectron spectroscopy (XPS) O 1*s* peaks of laser-processed and bare Si wafers, and h) XPS Si 2*p* peaks of laser-processed and bare Si wafers. The dashed lines in (h) denote deconvoluted curves of Si–Si and Si–O bonds of Si 2*p* peaks for the laser-processed Si wafer.

Table 1. XPS element analysis of the Si wafers without and with laser processing: binding energy; full width at half maximum (FWHM) of Si 2*p*, O 1*s* peaks, and O/Si atomic ratio.

Sample	Element	Binding energy [eV]	FWHM [eV]	[O]/[Si]
Bare Si wafer	Si 2*p*	99.36	1.39	0.009
	O 1*s*	532.14	2.65	
Laser-processed	Si 2*p*	99.34	1.44	0.156
	O 1*s*	532.26	2.6	

2.4. Light-Trapping Performance of Textured UT–Si

The size distribution of the pyramids in the nanotextured wafers was analyzed by image processing and shown in **Figure 5**a. The average size of the nanopyramids in terms of a pyramid basal width was 692 nm. For comparison, the Si wafers were also textured by a conventional KOH-texturing process and in the same manner, the size distribution of the pyramids was analyzed and shown in Figure 5b. The average size of the pyramids was 5.76 μm, which is a typical pyramid size produced in a standard KOH-texturing process. Effective light trapping in 50 μm thick UT c-Si wafers is more demanded compared with the case of a conventional solar grade wafers with a 200 μm thickness.[10,40] In Figure 5c, the total reflectance of 50 μm thick UT c-Si wafers with a planar surface, a typical micropyramid-textured surface, and a nanopyramid-textured surface by a laser-assisted texturing process are compared. It can be seen that the total reflectance of the nanopyramid-textured Si wafer is lower at a short wavelength of 400 nm or less, but slightly higher at a long wavelength of 800 nm or more compared with the micropyramid-textured Si wafer. The solar weighted reflectances for the micropyramid- and nanopyramid-textured sample were calculated and were 13.09% and 13.81%, respectively. The results show that the reflectance loss in the nanopyramid-textured sample is comparable to the micropyramid one. Additionally, the total reflectance of a sample deposited with single-layer antireflection coatings (SLARCs) of 75 nm ZnS on a nanopyramid-textured Si wafer and a double-layer ARC (DLARC) sample combining 105 nm MgF_2 and 52 nm ZnS were also measured and shown in Figure 5d.[41] The calculated weighted reflectance of the SLARC and DLARC structures was 6.72% and 4.82%, respectively. If the uniformity of the laser-assisted texturing process is improved in the future, the overall light-trapping performance of the nanopyramid texture can be improved.

2.5. Mechanical Flexibility of UT c-Si Wafers

To analyze the surface texturing effects on flexural strength, a four-point bending test was conducted using single-side textured Si wafers. Because of the catastrophic failure of the Si wafers, over 30 bending tests were conducted on each sample. A four-point bending test was performed using a bending jig with support and load spans of 8 and 4 mm, respectively, as illustrated in **Figure 6**a. The bending samples were fabricated 3 mm wide and 13 mm long by laser scribing after a surface-texturing process. Also, we also placed the textured surface on the support span to apply tensile deformation and analyze the effect of surface texturing effect on flexural strength. With a four-point bending test, the flexural strength can be calculated using Equation (1)[19,42]

$$\sigma_f = \frac{3PL}{4wt^2} \quad (1)$$

where P, L, w, and t are the fracture force, the distance between support spans, the width of the sample, and the sample thickness. Figure 6b shows the Weibull analysis based on results of four-point bending tests. Weibull analysis is a method for brittle materials such as silicon to analyze the stress distribution. Through Weibull analysis, characteristic strength (σ_0) and Weibull modulus (m) can be obtained for each texturing condition.

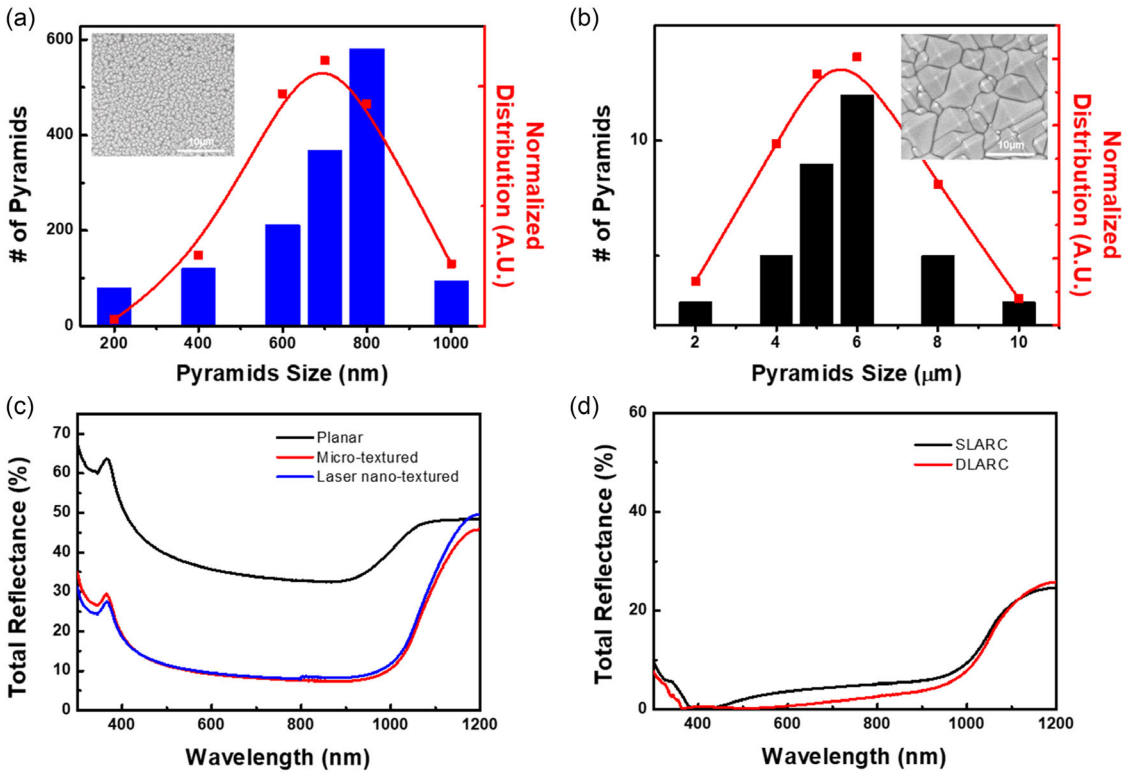

Figure 5. Comparison of micropyramid texturing and laser-assisted nanopyramid texturing: a) pyramid size distributions in the laser-assisted nanopyramid texturing, and b) pyramid size distributions in the micropyramid texturing. Inset figures in each figure show the SEM images of micropyramid and nanopyramid textures. c) The total reflectance of a planar surface, micropyramid surface and laser-assisted nanopyramid surface, d) the total reflectance of the laser-assisted nanopyramid surface with single-layer antireflection coating (SLARC) and double-layer antireflection coating (DLARC).

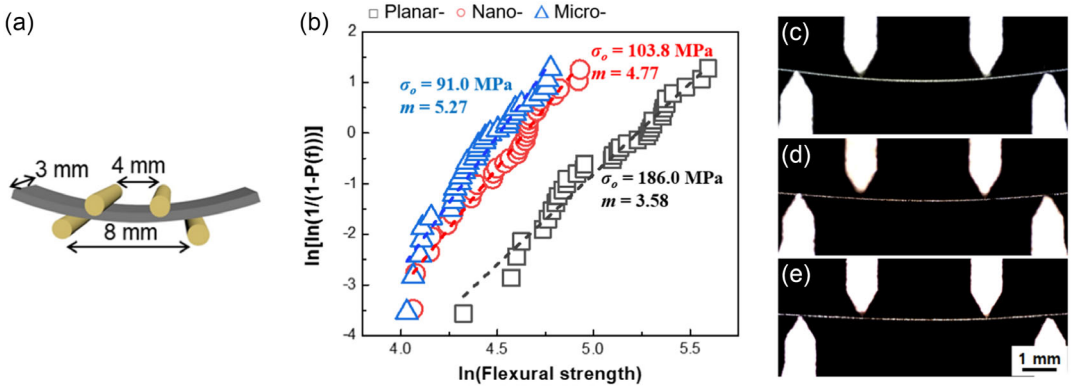

Figure 6. a) Schematic of a four-point bending test for ultrathin (UT) Si wafers. The strip ribbon represents a UT Si wafer with a 3 mm width. b) Weibull analysis of four-point bending tests, and critical bending radii of c) planar and d) nano- and e) microtextured silicon.

$$P(V_0) = \exp\left[-\left(\frac{\sigma - \sigma_u}{\sigma_0}\right)^m\right] \quad (2)$$

In Equation (2), $P(V_0)$, σ, and σ_u are the survival probability of the material, the applied stress, and the threshold stress, respectively. Threshold stress is equal to zero when the material has brittle fracture. Therefore, Equation (2) can be revised to Equation (3) and (4)

$$P(V_0) = \exp\left[-\left(\frac{\sigma - \sigma_u}{\sigma_0}\right)^m\right] \quad (3)$$

$$\ln\ln\left[\frac{1}{P(V_0)}\right] = m(\ln\sigma - \ln\sigma_0) \quad (4)$$

The characteristic strength and Weibull modulus can be obtained by Weibull distribution graph of Figure 6b and Equation (4).[43,44] The characteristic strength corresponds to a

survival probability of 37%, and Weibull modulus means distribution of the strength. Because Weibull modulus is obtained by slope of graph in Figure 6b, a lower value means a larger stress distribution. As a result of Weibull analysis, the characteristic strengths of non-, nano-, and microtextured Si wafers were 186.0, 103.8, and 91.0 MPa, respectively. The surface texture acts as a stress concentrator, and the strength of textured Si wafers is lowered. Based on previous research,[19,45] in case of a single notch, stress concentration is independent of notch angle when the notch angle is less than 90°, and notch depth and tip radius affects stress concentration. When the nano- and microtexture were compared, tip radii of nano- and microtexture were 29 and 28 nm, respectively. Also, the maximum notch depths of nano- and microtextures were 1 and 10 μm, respectively. Although the tip radii of nanotexture and microtexture are similar, the notch depth of microtexture is much deeper than that of nanotexture. Therefore, the characteristic strength of nanotextured Si samples was greater than that of microtextured Si samples. Weibull moduli of non-, nano-, microtextured samples are 3.58, 4.77, and 5.27, respectively. In other words, the stress distribution of non-textured Si samples is wider than that of textured Si wafers. It means that a flexural strength of non-textured Si samples is dominated by the highest stress concentrator that can be included stochastically. In case of textured samples, surface textures act as a highest stress concentrator, and they dominate in flexural strength. Also, Weibull modulus of microtextured Si samples is higher than that of nanotextured samples. It means that a larger stress concentration occurs in the micropyramidal texture. Figure 6c–e shows the images immediately before the fracture of three samples. Through these images, we obtained the critical bending radii. The critical bending radii were 27.2 (±6.6) mm for non-textured samples, 45.2 (±6.6) mm for nanotextured samples, and 53.9 (±12.5) mm for microtextured samples. The critical bending radius of nanotextured samples is 19.2% smaller than that of microtextured samples. All the parameters extracted from the four-point bending tests are summarized in **Table 2**.

2.6. Flexible UT-Passivated Emitter Rear Cell Solar Cells: Device Performances and Flexibility

Passivated emitter rear cells (PERCs) were fabricated with 50 μm thick UT c-Si wafers with a planar texture, a typical micropyramid texture, and a nanopyramid texture to compare their performances. The current–voltage characteristics measured under a standard solar irradiation of AM 1.5G with a 100 mW cm^{-2} light intensity are presented in **Figure 7**a. The external quantum efficiency (EQE) was also measured and is shown in Figure 7b. It can be divided into an SLARC structure and a DLARC structure, and the overall performances of the UT-PERC cell are shown in **Table 3**. For both SLARC and DLARC structures, the UT-PERC cell with nanopyramid textures showed the best efficiency. The average efficiency of the SLARC nanopyramid UT-PERC cell was 18.25%, which is 0.15% higher in absolute efficiency than the 18.10% efficiency of the micropyramid UT-PERC cell. The average efficiency of DLARC nanopyramid UT-PERC cells was 18.56%, which was 0.16% higher in absolute efficiency than the 18.40% efficiency of micropyramid UT-PERC cells. Apart from the ARC structure, it was confirmed that the difference between nanopyramid and micropyramid showed a similar efficiency difference of about 0.15%. The champion cell that showed the highest efficiency was a DLARC nanopyramid UT-PERC cell with an efficiency of 18.68%. A closer look at the characterization parameters of the nanopyramid and micropyramid UT-PERC cells shows that there is no significant difference in V_{oc}, the cells of the micropyramid structure are higher in J_{sc}, and the cells of the nanopyramid structure are superior in FF. These results are thought to be due to the emitter formation properties of the nanostructures. The emitter profile formed in the nanopyramid has a higher surface density and deeper junction depth than the conventional textured, which may be responsible for the lower current density and superior FF of the nanopyramid UT-PERC cells. The current density–voltage (J–V) curves and EQE results in Figure 7a,b show only the results of the champion device among the DLARC PERC cells with different surface conditions. The efficiency (18.68%) we achieved with the nanopyramid-textured UT-PERC cells is among the highest values especially for laser-textured Si solar cells. The black Si solar cells textured by pulse laser have been challenged to achieve high efficiency due to surface passivation of high aspect ratio Si nanostructures as reported by many research groups.[30,46–48] In contrast to the previous research, we fabricated nanoscale pyramidal texture of relatively lower aspect ratio, which allows for more effective surface passivation.

Bending radius testing with the fabricated UT-PERC cells was performed using the specially designed bending test jigs with different bending radius shown in Figure S3, Supporting Information, to check if the result of the flexibility experiment conducted through the bare wafer has any difference in the actual cell stage. Each UT-PERC cell has a planar surface, a typical micropyramid-textured surface, and a nanopyramid-textured surface, which can be used to identify the critical bending radius at which cell fracture occurs. Interesting results from critical bending radius tests of UT-PERC cells with different surface structures can be seen in Figure 7c. A critical bending radius of the planar UT-PERC cells were 26 mm, micropyramid UT-PERC cells were 28 mm, and a critical bending radius of nano-pyramid UT-PERC cells were 26 mm, respectively. The nanopyramid UT-PERC cells reduced the critical bending radius by 2 mm compared with micropyramid UT-PERC cells. The critical bending radius of nano-pyramid UT-PERC cells was found to be equivalent to that of planar UT-PERC cells, but it is necessary to look more closely at the 28 mm test results. When looking at the test results at a bending radius of 28 mm where the fracture started, planar samples had a breakage probability of 50%, while nanopyramid samples had a breakage probability of 40%. The critical bending radius test results of these UT-PERC cells are

Table 2. Weibull modulus (m), critical bending radius (R_{crit}), and characteristic strengths (σ_0) of UT–Si wafers by Weibull distribution analysis.

Parameters	Planar	Nanotexture	Microtexture
m	3.58	4.77	5.27
σ_0 [MPa]	186.0	103.8	91.0
$R_{crit.}$ [mm]	27.2 (±6.6)	45.2 (±6.55)	53.9 (±12.5)

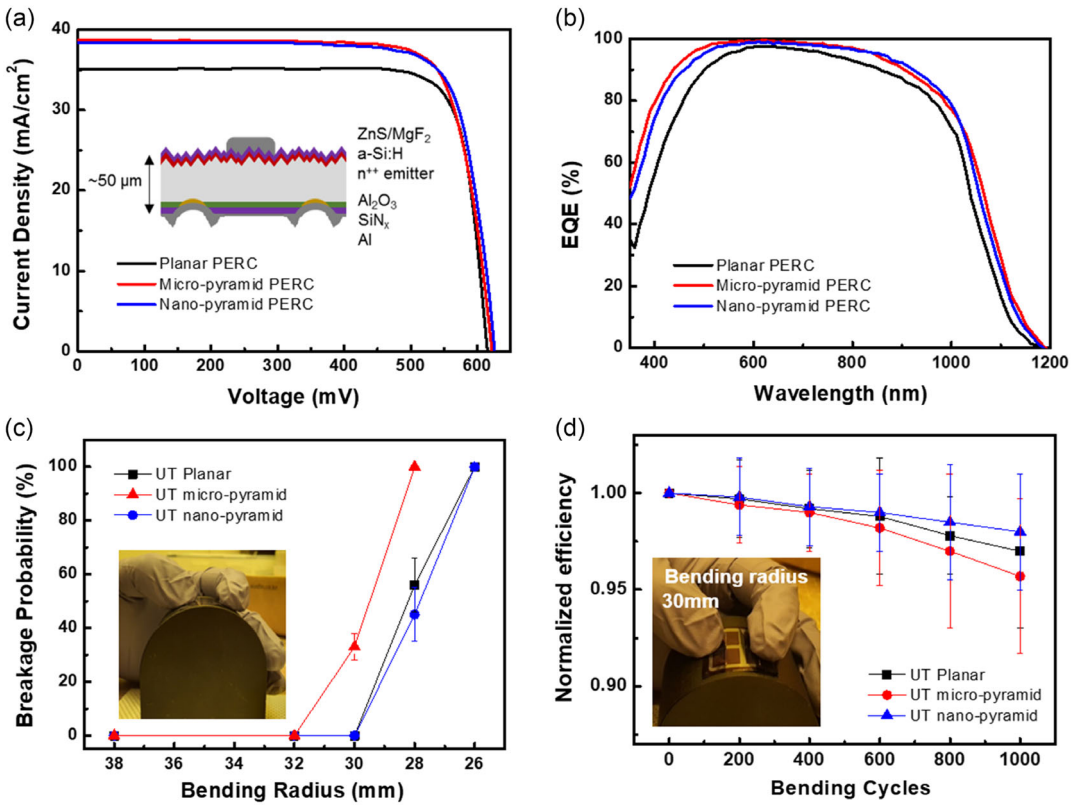

Figure 7. a) Current density–voltage (J–V) characteristic curves of DLARC UT-passivated emitter rear cell (UT-PERC) cells with different surface structures. A cell structure is illustrated in the inset figure. b) External quantum efficiency (EQE) results of DLARC UT-PERC cells with different surface structures. c) Breakage probability results of DLARC UT-PERC cells with different surface structures. d) Efficiency degradation depending on the bending cycle of DLARC UT-PERC cells with different surface structures. Inset figures in (c) and (d) show a bending test jig.

Table 3. Performance parameters of the UT–Si wafer-based solar cells with various textures and ARCs. The champion cell performance parameters in each cell are shown in parentheses.

ARC	Texture	V_{oc} [mV]	J_{sc} [mA cm]$^{-2}$	FF [%]	Eff [%]
SLARC	Planar	619.00 ± 2.40 (622)	33.84 ± 0.34 (34.29)	76.18 ± 0.30 (76.35)	15.96 ± 0.25 (16.28)
	Micro	620.80 ± 2.53 (622)	38.01 ± 0.28 (38.25)	76.84 ± 0.20 (76.88)	18.10 ± 0.11 (18.31)
	Nano	622.00 ± 2.80 (628)	37.66 ± 0.20 (37.65)	78.00 ± 0.22 (77.91)	18.25 ± 0.10 (18.33)
DLARC	Planar	618.20 ± 1.79 (621)	35.14 ± 0.13 (35.18)	76.13 ± 0.10 (76.12)	16.54 ± 0.10 (16.63)
	Micro	620.33 ± 1.86 (623)	38.54 ± 0.12 (38.56)	76.96 ± 0.08 (77.12)	18.40 ± 0.10 (18.53)
	Nano	620.14 ± 2.03 (624)	38.34 ± 0.10 (38.32)	78.08 ± 0.14 (78.13)	18.56 ± 0.17 (18.68)

consistent with the previous four-point bending test results. The nanopyramid samples clearly show higher mechanical flexibility than the micropyramid samples. The nanopyramid samples do not show a significant difference compared to the planar samples but show slightly improved mechanical flexibility. In the additional cycle bending test, as shown in Figure 7d, micropyramid UT-PERC cells showed a decrease in efficiency of 4.3% compared to the initial efficiency after 1000 bending tests, whereas planar UT-PERC cells and nanopyramid UT-PERC cells showed a decrease in efficiency of 3.0% and 2.0%, respectively. As shown in Figure S7, Supporting Information, this decrease in efficiency after the cycle bending test is mainly due to the decrease in FF and series resistance. It is thought that the series resistance increased as the electrode was damaged during the bending test.

Mechanical properties such as flexural strength are known to be sensitive to the surface textures of Si wafers and dependent on the wafer thickness.[19,49] In the literature, a 50 μm thick microwire-textured UT Si wafers exhibited a low bending radius of 12 mm.[13] Recently, the excellent flexibility of a 60 μm thick Si wafers with a 4 mm critical bending radius was reported.[36] Flexibility was improved by blunting micropyramidal textures at the regions rather than the whole wafer. The critical bending radius of our UT-Si solar cells is larger than the reported data, we

expect to reduce the critical bending radius by adopting the similar approach.

3. Discussion

3.1. Laser-Assisted Nanotexturing Mechanism

As mentioned in the results part, the role of the nanolens is to concentrate the light passing through the lens. It is essential to identify a process window that can optimize the laser irradiation condition to achieve a uniform and dense texture shape without damaging the nanolens. Figure S4, Supporting Information, demonstrates that when the laser fluence is too low, a uniformly textured surface cannot be obtained in a short amount of time even if a nanolens is used. Conversely, if the laser fluence is too strong such as in the case of 7.13 J cm^{-2}, the nanolens is damaged, and the shape of the texture surface is altered, so the nanopyramids are not formed. Therefore, finding the appropriate laser fluence condition is crucial for achieving the desired texture shape while preserving the nanolens for the reuse. Through experiments, the critical power for laser-assisted nanotexturing using a nanolens was determined to be 4.1 J cm^{-2}, and the optimal laser condition for the most uniform texturing was 5.5 J cm^{-2}. Looking at the results of Figure S4, Supporting Information, along with the laser power condition, it was found that the density of initial pyramidal nucleation was related to the number of the laser scans. When analyzing particles using Image-J, it becomes evident that the number and density of pyramidal nuclei generated in the beginning of the texturing process increase as the number of laser scans increases from 1 to 3 and 5 times. Recall that the laser-assisted texturing process causes the local heating on the Si wafer by a focused laser beam through the nanolens, creating a unique spherical SiO_2 mask on the Si surface. The distribution of these unique spherical SiO_2 masks can be seen through the atomic force microscopy image in Figure S6, Supporting Information. Analyzing the distribution of these unique spherical SiO_2 masks, it can be confirmed that the spacing between the SiO_2 masks is about 775 nm, similarly to the spacing of our nanolens. As previously mentioned, the unique spherical SiO_2 masks generated by the nanolens make the initial pyramidal nucleation fast and dense when the Si wafer is textured in a KOH solution. It is a key factor in achieving a uniform nanopyramid surface within a short time frame of 90 s.

3.2. Finite-Element Method Simulation and Mechanical Flexibility

The cross-sectional SEM images of the nano- and microtextured Si wafers in the same scale are presented in **Figure 8**a,b. Finite-element analysis (FEA) simulations were conducted to analyze the stress concentration and distribution of micro- and nanotextured samples. As shown in Figure 8c,d, the maximum stress is concentrated on microtexture, which has highest depth for microtextured sample. In contrast, in periodic nanotextured samples, the stress is distributed by around texture, and the stress concentration effect is less than that of microtextured samples. Through FEA results, a stress concentration factor (SCF) was calculated using the following equation[19,44]

$$K = \frac{\sigma_{\max}}{\sigma_{\text{nom}}} \tag{5}$$

where K is an SCF, and $\sigma_{\max}$ is a maximum stress at the notch tip. σ_{nom} is the nominal stress far from the texture. Stress concentration factors analyzed by four-point bending tests were 1.79 for nanotextured samples and 2.05 for microtextured samples. Calculated SCFs based on the FEA results were 6.13 for nanotextured samples and 8.27 for microtextured samples. Because the FEA simulations were performed using 2D models, stress

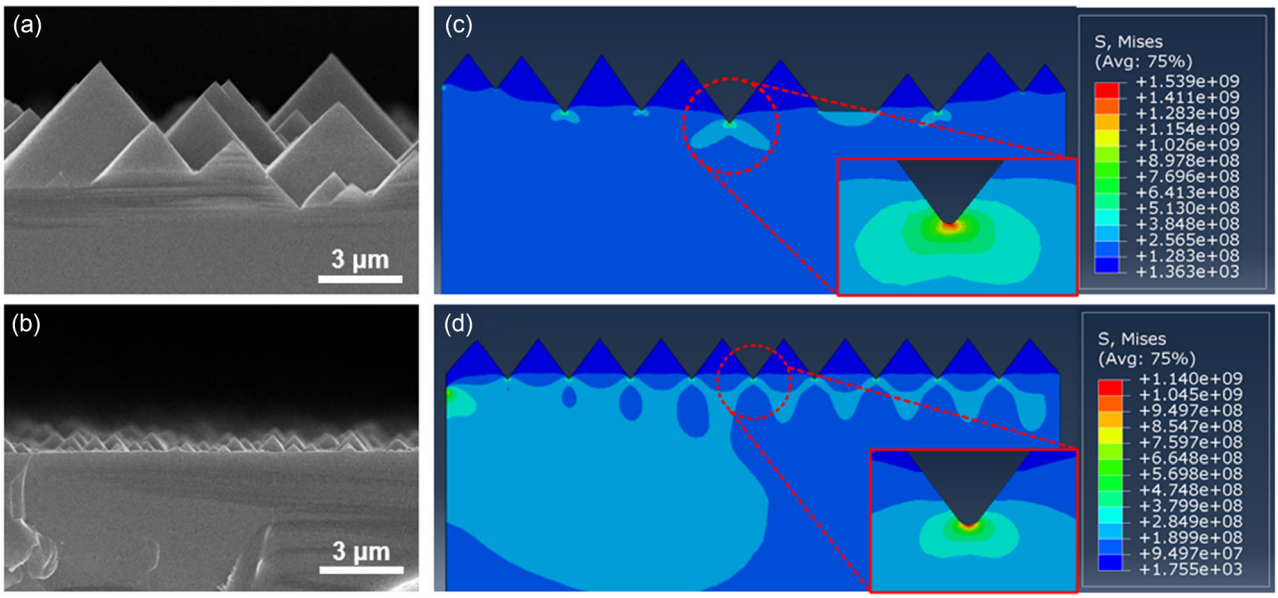

Figure 8. Cross-sectional SEM images of a) micropyramid and b) nanopyramid Si wafers. Finite-element analysis (FEA) simulation results of c) microtextured and d) nanotextured UT–Si wafers.

dispersion does not occur effectively. Therefore, the calculated SCF is higher than the measured SCF. From the experimental bending results and the FEA simulations, it was found that stress was dispersed effectively in nanotextured Si wafers, which means the flexibility of nanotextured samples is better than that of microtextured samples due to the stress dispersion effect.

4. Conclusion

In summary, we have developed a laser-assisted nanotexturing process using an HSQ film as a nanolens to focus a pulse laser onto UT–Si wafers. The focused laser induces silicon oxide nanoparticles on the UT–Si wafers, which serve as etch mask in alkaline solution for nanoscale pyramid texturing. The mechanical flexibility of the UT–Si wafers–textured random pyramid structures was analyzed by a four-point bending test and compared with planar UT–Si wafers. We introduced the nanoscale pyramid textures on the UT–Si-based cell fabrication in the PERC architecture. The PERC solar cells, which are currently a mainstream technology in the PV industry, were manufactured using 50 μm thick UT c-Si wafers with different surface textures, and their performance was verified. Through this experiment, we lead to a conclusion that the mechanical flexibility of the UT–Si wafers with the nanopyramid textures is excellent compared to the planar and typical micropyramid-textured wafers. In addition, the PERC flexible solar cells maintain their efficiency under 1000 cyclic bending tests with a 30 mm bending radius. Therefore, we believe that the laser-texturing technology using the nanolens we proposed can be a promising candidate for the manufacture of a thin flexible solar cell.

5. Experimental Section

Fabrication Process of Nanolens: To prepare the SNS solution, powders of 960 nm diameter spherical silica beads (Bang Laboratory) were dispersed in a binary solution *N,N*-dimethyl formamide (anhydrous 99.8%, Sigma–Aldrich) and ethylene glycol (anhydrous 99.8%, Sigma-Aldrich) = 9:1, v/v] at a silica-bead concentration of 400 mg mL^{-1}. The solutions were sonicated for 5 h to produce complete dispersion of the SNS. Test substrates consisting of Si wafers (1–5 Ω cm, p-type, czochralski (CZ), 525 μm thick) of a (100) crystal orientation of square pieces (30 × 30 mm) were washed in acetone, methanol, and ethanol with sonication for 15 min and rinsed in deionized water for 10 min. To form a hydrophilic Si surface, they were subsequently cleaned in a piranha solution [H_2SO_4 (95%):H_2O_2 (30%) = 3:1] for 20 min followed by 10 min deionized water rinse. The SNS solution of 150 μL was dropped and spun onto the clean Si substrates using a spin coater at 2000 rpm for 270 s, producing a self-assembled monolayer of SNS in a hexagonal close-packed array. The RIE process was performed using SF_6 and O_2 gas with the SNS monolayer serving as the etch mask. The Si master sample to be used for NIL was completed by a 5 min at a SF_6:O_2 partial pressure ratio of 8:2 RIE process. Subsequently, the master sample was coated with fluorine, poured with PDMS, and baked at 90 °C for 1 h to form a pattern. Then, the HSQ resin was spun on the PDMS mold and pressed together with the glass substrate to fabricate a nanolens. The fabricated nanolens was subjected to additional UV treatment, and heat treatment at 400 °C for 1 h was performed for curing and shape control. Please refer to Figure 1 for the overall process.

Laser-Assisted Texturing: The fabricated nanolens was placed on a Si wafer with a size of 30 × 30 mm in the air, which was then irradiated using a diode-pumped Q-switched Nd:YVO_4 laser with a 20 ns duration at a 532 nm wavelength. To minimize vibrations, the sample stage was placed on an anti-vibrating table during the experiment. The chosen laser fluence was 5.5 J cm^{-2}, and the wafer was scanned with a laser five times. The laser diode current was set to 25 A, the laser frequency was set to 60 kHz, and the spacing between lines was set to 8 μm in the line scan mode. The laser beam size was 16 μm, and the laser scan speed was adjusted to obtain the same overlapping in the vertical and horizontal scan directions. Following laser irradiation, the samples were immersed in a 25 wt% HF solution for 30 s to remove the SiO_2 layer. Subsequently, they were etched for 90 s in a 10 wt% KOH solution at 70 °C along with an additive (SEA, Sunflower 100). After KOH etching, the Si substrates were rinsed in deionized water for 1 min and rinsed in a 25 wt% HF solution for 30 s.

Four-Point Bending Test: Non-, nano-, and microtextured samples were prepared for bending tests. Four-point bending test samples were fabricated by laser scribing with a width of 3 mm and a length of 13 mm. The four-point bending tests were performed using a universal testing machine (Instron 5948) at a loading rate of 5 μm s^{-1}. Textured surfaces of the Si wafers were placed to face the support span to apply tensile deformation. During the bending test, video was recorded, and the critical bending radius was measured by capturing an image immediately before the fracture. All experiments were conducted under laboratory conditions.

FEA Simulations: The FEA simulations were conducted to analyze the stress distribution and concentration in relation to surface texturing. Abaqus 6.14 and Abaqus CAE were used for FEA simulations and creation of input files, respectively. The simulations were performed for force control and linear elasticity condition. A 2D deformable shell model was used, and the sketch used in the FEA simulation was identical to the typical SEM fracture images of textured samples (Figure 8a,b). The mechanical properties of silicon were input based on previous research findings.[50,51]

Cell Fabrication and Cycle Bending Test: For the fabrication of UT c-Si PERC cells, the (100) oriented *p*-type CZ Si wafers with a resistivity of 1 − 3 Ωcm and a 50 μm thickness of square pieces (30 mm × 30 mm) were cleaned with RCA1 and RCA2 solutions. Laser-assisted texturing was performed on both sides, and a SiO_2 diffusion barrier of 200 nm was deposited on the rear side using PECVD. A $POCl_3$ tube furnace was used to form a diffused emitter of a 100 Ω sq^{-1} sheet resistance. The phosphor-silicate glass on both sides was removed by HF solution. A 20 nm thick aluminum oxide (Al_2O_3) layer was deposited on the rear side using atomic layer deposition for passivation, followed by an 80 nm thick SiN_x capping layer using PECVD. A SF_6 RIE etch process was used to isolate four neighboring cells of 10 × 10 mm. A 10 nm thick hydrogenated amorphous Si(a-Si:H) layer was used as a passivation layer on the emitter. A local contact structure was formed by opening the a-Si:H layer locally using photolithography and HF/nitric/acetic acid solution. The sub-cells were finalized by depositing a 2 μm thickness thick aluminum (Al) layer for the rear electrode using e-beam evaporation, and the rear contact was formed through a laser-fired contact process using a diode-pumped Q-switched Nd:YVO_4 laser. An 800 nm thick Ag front electrode was formed using photolithography and lift-off process. Zinc sulfide (ZnS) was deposited by 75 nm thermal evaporation for SLARC, and ZnS 52 nm and magnesium fluoride (MgF_2) 105 nm were deposited by thermal evaporation for DLARC. The solar cells were tested under standard solar irradiation of AM 1.5 G at a 100 mW cm^{-2} light intensity using a solar simulator (Oriel LSC-100), and their performance parameters were determined from the current–voltage characteristics. The EQE was also measured in a wavelength range from 350 to 1150 nm.

The cycle bending test was carried out using a specially designed bending test jig with a bending radius of 30 mm. UT-PERC cells with planar surface, micropyramid surface, and nanopyramid-textured surface were tested with four samples of each cell structure. All samples were subjected to a total of 1000 bending tests, and solar cell parameters were measured using a solar simulator after every 200 bending cycles. All the results of the cycle bending test can be seen in Figure S7, Supporting Information.

Supporting Information

Supporting Information is available from the Wiley Online Library or from the author.

Acknowledgements

Y.L. and J.-H.W. contributed equally to this work. This work was partly supported by KIST (Korea Institute of Science and Technology) institutional program and the Korea Institute of Energy Technology Evaluation and Planning (KETEP) grant funded by the Korean government (MOTIE) (grant nos. 20213091010010 and 20228520010020). I.K. and D.-K.L. acknowledged the financial support from the National Research Foundation of Korea (grant no. 2019K1A3A1A61091348).

Conflict of Interest

The authors declare no conflict of interest.

Author Contributions

Y.L.: Methodology, Investigation, Data curation, Writing—original draft. J.-H.W.: Methodology, Investigation, Writing—original draft. K.K.: Writing—review & editing. K.L.: Investigation, Methodology. Y.J.: Investigation, Validation. J.K.: Investigation, Validation. Gyu W.H.: Writing—review & editing. D.-K.L.: Funding acquisition, Writing—review & editing. J.-Y.K.: Co-supervision, Conceptualization, Methodology, Writing—review & editing. I.K.: Supervision, Funding acquisition, Writing—review & editing.

Data Availability Statement

The data that support the findings of this study are available from the corresponding author upon reasonable request.

Keywords

flexible solar cells, mechanical bending test, nanopyramid texturing, nanosecond pulse laser, ultrathin crystalline Si

Received: May 16, 2023
Revised: July 17, 2023
Published online: August 6, 2023

[1] K. X. Wang, Z. Yu, V. Liu, Y. Cui, S. Fan, *Nano Lett.* **2012**, *12*, 1616.
[2] J. He, P. Gao, M. Liao, X. Yang, Z. Ying, S. Zhou, J. Ye, Y. Cui, *ACS Nano* **2015**, *9*, 6522.
[3] G. Bye, B. Ceccaroli, *Sol. Energy Mater. Sol. Cells* **2014**, *130*, 634.
[4] M. A. Woodhouse, B. Smith, A. Ramdas, R. M. Margolis, United States **2019**.
[5] A. Louwen, W. van Sark, R. Schropp, A. Faaij, *Sol. Energy Mater. Sol. Cells* **2016**, *147*, 295.
[6] M. A. Green, *Sol. Energy Mater. Sol. Cells* **2008**, *92*, 1305.
[7] W. Hadibrata, F. Es, S. Yerci, R. Turan, *Sol. Energy Mater. Sol. Cells* **2018**, *180*, 247.
[8] S. Wang, B. D. Weil, Y. Li, K. X. Wang, E. Garnett, S. Fan, Y. Cui, *Nano Lett.* **2013**, *13*, 4393.
[9] S. Zhou, Z. Yang, P. Gao, X. Li, X. Yang, D. Wang, J. He, Z. Ying, J. Ye, *Nanoscale Res. Lett.* **2016**, *11*, 194.
[10] K. J. Yu, L. Gao, J. S. Park, Y. R. Lee, C. J. Corcoran, R. G. Nuzzo, D. Chanda, J. A. Rogers, *Adv. Mater.* **2013**, *3*, 1401.
[11] M. Pagliaro, R. Ciriminna, G. Palmisano, *ChemSusChem* **2008**, *1*, 880.
[12] I. Hwang, Y. Jeong, Y. Shiratori, J. Park, S. Miyajima, I. Yoon, K. Seo, *Cell Rep. Phys. Sci.* **2020**, *1*, 100242.
[13] I. Hwang, H.-D. Um, B.-S. Kim, M. Wober, K. Seo, *Energy Environ. Sci.* **2018**, *11*, 641.
[14] E. Garnett, P. Yang, *Nano Lett.* **2010**, *10*, 1082.
[15] J. He, Z. Yang, P. Liu, S. Wu, P. Gao, M. Wang, S. Zhou, X. Li, H. Cao, J. Ye, *Adv. Mater.* **2016**, *6*, 1501793.
[16] A. Mavrokefalos, S. E. Han, S. Yerci, M. S. Branham, G. Chen, *Nano Lett.* **2012**, *12*, 2792.
[17] Y. Lee, Y. Woo, D.-K. Lee, I. Kim, *Sol. Energy* **2020**, *208*, 957.
[18] S. E. Han, G. Chen, *Nano Lett.* **2010**, *10*, 4692.
[19] J.-H. Woo, Y.-C. Kim, S.-H. Kim, J.-I. Jang, H. N. Han, K. J. Choi, I. Kim, J.-Y. Kim, *Scr. Mater.* **2017**, *140*, 1.
[20] X. Tan, W. Yan, Y. Tu, C. Deng, *Opt. Express* **2017**, *25*, 14725.
[21] Y. Lu, A. Lal, *Nano Lett.* **2010**, *10*, 4651.
[22] P. B. Fischer, S. Y. Chou, *Appl. Phys. Lett.* **1993**, *62*, 1414.
[23] Y. Chen, *Microelectron. Eng.* **2015**, *135*, 57.
[24] L. Zhao, Z. Wang, J. Zhang, L. Cao, L. Li, Y. Yue, D. Li, *Appl. Surf. Sci.* **2015**, *346*, 574.
[25] H.-S. Lee, J. Suk, H. Kim, J. Kim, J. Song, D. S. Jeong, J.-K. Park, W. M. Kim, D.-K. Lee, K. J. Choi, B.-K. Ju, T. S. Lee, I. Kim, *Sci. Rep.* **2018**, *8*, 3504.
[26] T. Mårtensson, P. Carlberg, M. Borgström, L. Montelius, W. Seifert, L. Samuelson, *Nano Lett.* **2004**, *4*, 699.
[27] Z. Yu, H. Gao, W. Wu, H. Ge, S. Y. Chou, *J. Vac. Sci. Technol., B* **2003**, *21*, 2874.
[28] J. C. Zolper, S. Narayanan, S. R. Wenham, M. A. Green, *Appl. Phys. Lett.* **1989**, *55*, 2363.
[29] D. Zielke, D. Sylla, T. Neubert, R. Brendel, J. Schmidt, *IEEE J. Photovoltaics* **2013**, *3*, 656.
[30] M. Abbott, J. Cotter, *Prog. Photovoltaics: Res. Appl.* **2006**, *14*, 225.
[31] Q. Wang, W. Zhou, *Opt. Mater.* **2017**, *72*, 508.
[32] S. Kontermann, T. Gimpel, A. L. Baumann, K. M. Guenther, W. Schade, *Energy Procedia* **2012**, *27*, 390.
[33] X. Liu, P. R. Coxon, M. Peters, B. Hoex, J. M. Cole, D. J. Fray, *Energy Environ. Sci.* **2014**, *7*, 3223.
[34] J. Y.-H. Chai, B. T. Wong, S. Juodkazis, *Mater. Today Energy* **2020**, *18*, 100539.
[35] C.-C. Lin, Y.-J. Chuang, W.-H. Sun, C. Cheng, Y.-T. Chen, Z.-L. Chen, C.-H. Chien, F.-H. Ko, *Microelectron. Eng.* **2015**, *145*, 128.
[36] W. Liu, Y. Liu, Z. Yang, C. Xu, X. Li, S. Huang, J. Shi, J. Du, A. Han, Y. Yang, G. Xu, J. Yu, J. Ling, J. Peng, L. Yu, B. Ding, Y. Gao, K. Jiang, Z. Li, Y. Yang, Z. Li, S. Lan, H. Fu, B. Fan, Y. Fu, W. He, F. Li, X. Song, Y. Zhou, Q. Shi, et al., *Nature* **2023**, *617*, 717.
[37] S.-E. Cheon, H.-S. Lee, J. Choi, A. R. Jeong, T. S. Lee, D. S. Jeong, K.-S. Lee, W.-S. Lee, W. M. Kim, H. Lee, I. Kim, *Sci. Rep.* **2017**, *7*, 7336.
[38] H.-S. Lee, G.-W. Hwang, T.-Y. Seong, J. Park, J. W. Kim, W. M. Kim, I. Kim, K.-S. Lee, *Sci. Rep.* **2021**, *11*, 12218.
[39] A. S. M. Mohsin, M. Mobashera, A. Malik, M. Rubaiat, M. Islam, *J. Opt.* **2020**, *49*, 523.
[40] L. C. Andreani, A. Bozzola, P. Kowalczewski, M. Liscidini, L. Redorici, *Adv. Phys. X* **2019**, *4*, 1548305.
[41] S. L. Diedenhofen, G. Grzela, E. Haverkamp, G. Bauhuis, J. Schermer, J. G. Rivas, *Sol. Energy Mater. Sol. Cells* **2012**, *101*, 308.
[42] J. S. Lee, S. Kwon, H. Park, Y. D. Kim, H.-J. Kim, H. Lim, S. Yoon, D. Kim, *Korean J. Mater. Res.* **2009**, *19*, 18.
[43] L. Ćurković, A. Bakić, J. Kodvanj, T. Haramina, *Trans. FAMENA* **2010**, *34*, 13.
[44] K. Kashyap, A. Kumar, C.-T. Huang, Y.-Y. Lin, M. T. Hou, J. Andrew Yeh, *Sci. Rep.* **2015**, *5*, 10869.
[45] W. D. Pilkey, D. F. Pilkey, Z. Bi, *Peterson's Stress Concentration Factors*, John Wiley & Sons, Hoboken NJ **1997**.
[46] B. K. Nayak, V. Iyengar, M. C. Gupta, *MRS Online Proc. Lib. (OPL)* **2008**, *1123*, 1123.

[47] V. V. Iyengar, B. K. Nayak, M. C. Gupta, *Sol. Energy Mater. Sol. Cells* **2010**, *94*, 2205.
[48] V. V. Iyengar, B. K. Nayak, M. C. Gupta, *Sol. Energy Mater. Sol. Cells* **2010**, *94*, 2251.
[49] Y. Hara, K. Ide, T. Nishihara, R. Yokogawa, K. Nakamura, Y. Ohshita, T. Kawatsu, T. Nagai, Y. Aoki, H. Kobayashi, N. Yamada, Y. Miyashita, A. Ogura, *Jpn. J. Appl. Phys.* **2023**, *62*, 017001.
[50] S. Goel, A. Kovalchenko, A. Stukowski, G. Cross, *Acta Mater.* **2016**, *105*, 464.
[51] T. Vodenitcharova, O. Borrero-López, M. Hoffman, *Acta Mater.* **2012**, *60*, 4448.